Energy 236 (2021) 121405

Contents lists available at ScienceDirect

Energy

journal homepage: www.elsevier.com/locate/energy

A critical analysis of shale laboratory permeability evolution data

Rui Shi [a, b], Jishan Liu [c], Xiaoming Wang [b, *], Mingyao Wei [d], Derek Elsworth [e]

[a] School of Resources and Geosciences, China University of Mining and Technology, Xuzhou, 221116, China
[b] Key Laboratory of Tectonics and Petroleum Resources, Ministry of Education, China University of Geosciences, Wuhan, 430074, China
[c] Department of Chemical Engineering, School of Engineering, The University of Western Australia, 35 Stirling Highway, WA, 6009, Australia
[d] IoT Perception Mine Research Center, China University of Mining & Technology, Xuzhou, 221116, China
[e] Department of Energy and Mineral Engineering, G3 Centre and Energy Institute, The Pennsylvania State University, University Park, PA, 16802, USA

ARTICLE INFO

Article history:
Received 12 January 2021
Received in revised form
5 June 2021
Accepted 1 July 2021
Available online 3 July 2021

Keywords:
Shale permeability
Microstructural characteristics
Permeability bounds
Effective stress
Gas slippage

ABSTRACT

This review study aims to identify why current experimental measurements of shale permeability are not consistent with predictions of commonly-used permeability models and explore how the identified reason would guide future research. These goals are achieved through the collection of experimental permeability measured under constant confining pressure (CCP) and constant effective stress (CES) conditions. These data show that permeability ratios (k/k_0) vary between an upper bound and a lower bound. A generic permeability model is developed to delineate the boundaries of k/k_0 based on shale microstructural characteristics. It's found that for upper bounds are controlled primarily by the fracture behavior while for lower bounds are controlled by the matrix or intact shale behavior. These findings suggest that the model predictions represent only behaviors of either fracture system or matrix while the experimental measurements from CCP and CES observations are for real shales. For real shales the internal dependencies among these factors cannot be fully understood through the nature of the external boundary conditions in CCP and CES tests, alone, but require high-level knowledge of sample structure and process interactions. The nature of permeability time dependencies on the internal process interactions must be reflected in any future experimental and modeling research.

1. Introduction

Global energy consumption increased considerably in the last decades as the result of population growth and economic development, of which natural gas accounts for a quarter of the total energy demand [1–3]. For past decades, unconventional resources have been emerged as a resource of substantial importance in the world for shares of conventional gas and oil production [4,5]. For example, shale gas is the largest contributor to natural gas production in United States, and it is predicted to account for almost two-thirds of total American gas production by 2040 [6]. Shale is a typical dual porosity system composed of fracture and matrix, with the latter consisting of organic matter (kerogen) and inorganic nanotube scale capillaries [7–18]. Gas resides in these complex porous system swells with gas adsorption and shrinks with gas desorption [19–22]. These characteristics determine the peculiarities of shale permeability evolution and have an inherent link with the production behavior of shale gas reservoirs [23]. Therefore, it is important to study the evolution of shale permeability during the production process.

A broad variety of laboratory experiments has been carried out to study the evolution of shale permeability [24]. Two types of experiments, *viz.* constant confining pressure (CCP) and constant effective stress (CES) tests, are widely conducted to investigate the impact of various factors, including gas sorption, effective stress and slippage. In CCP tests, the total confining stress is kept constant, while the effective stress is constant in CES tests. When the total confining stress is constant, the gas sorption, effective stress and slippage are believed to exert important controls on the evolution of shale permeability. When the effective stress is constant, gas sorption and slippage effects is considered to be the primary factors in controlling the evolution of shale permeability. The fundamental assumption behind this approach is that the impacts of effective stress, gas sorption-induced matrix swelling/shrinking and slippage effects on shale permeability could be separated and investigated individually [25–27]. This assumption also applies to tests conducted under conditions of constant pore pressure [28–41].

The main objective of CCP tests is to understand the influence of

* Corresponding author.
E-mail address: sunwxm@cug.edu.cn (X. Wang).

https://doi.org/10.1016/j.energy.2021.121405
0360-5442/

effective stress and gas sorption on the evolution of shale permeability. For example, CCP tests have been used to determine the influence of effective stress and the impact of adsorption [30,42–44], artificial fractures on permeability [43,45,46] and slippage effect on permeability [25,32,42,47–51]. In these studies, the evolution of shale permeability data can be classified into two categories: permeability increases directly with the increase of injection pore pressure; permeability decreases initially with the increase of injection pore pressure and shows only minimal rebound.

CES tests aim to measure the influence of slippage effect and associated effects, such as gas adsorption/desorption, on the evolution of shale permeability. For example, CES tests have been used to investigate the impact of gas adsorption/desorption on the evolution of permeability [52–57], to characterize the influence of slippage effect [31,42,49,53–56,58–67] and the magnitude of effective stress on permeability [31,58,59,63]. These studies indicate that shale permeabilities recovered from CES tests, decrease with an increase in pore pressure.

A variety of permeability models have been developed to explain the experimental observations of shale permeability from both CCP and CES tests. These models can be classified into two groups: stress-independent apparent permeability (SIAP) models and stress-dependent apparent permeability (SDAP) models. The SIAP models [68–71] are used to explain experimental data for cases where the development of nanopores in the shale matrix is more important. In these models [68,69] the intrinsic permeability, k_∞, is treated as a constant. For stress sensitive cases, SDAP models [24,42,72–75] are developed based on the poroelastic theory.

Gas sorption, effective stress and slippage can affect the evolution of shale permeability. Under conditions of constant confining pressure, effective stresses decrease as the gas pressure increases. This reduction in effective stress results in a concomitant increase in permeability, while the slippage effect would cause the apparent permeability to decrease in the low pore pressure regime [76]. In the high pore pressure regime, the influence of slippage effect is greatly reduced, then with the decrease of effective stress the permeability is expected to increase with the increased pore pressure [72]. While not all experimental results meet these expectations. For example, under the same pore pressure, the permeability to a non-adsorbing gas (such as helium) is always greater than that to an adsorbing gas (like methane) [25,47,52,56]. Then there is a gap that the adsorption of gases on the pore surface can reduce about a few nanometers of the radius of pores, cannot develop such a significant decrease [77]. In both CCP and CES tests, an implicit assumption of pressures equilibrated in both matrix and fracture (or bigger pores and dense matrix blocks) is employed when the permeability is measured. Under this assumption, the gas pressure in the fracture system is in equilibrium with that in the matrix system, and the process interactions among matrix (multi-scale pore) and fracture have reached a dynamic equilibrium state. Permeability models are also derived under the same assumption. If this equilibrium state is not yet reached when the permeability measurements are taken, the experimental results may not be consistent with the key assumption of equilibrium-pore-pressure-based permeability models [78–80].

In this study, we collected and critically examined experimental permeability data from both CCP and CES tests to define key controls on response and to develop a generic permeability model to represent permeability evolution.

2. Review of shale laboratory test permeability data

2.1. Review of constant confining pressure test data

Experimental permeability data were collected from a variety of CCP tests. In those experiments, the confining pressure was maintained while the effective stress was gradually decreased [45].

In the CCP tests, gas permeability was measured either by steady-state or pressure transient tests and calculated using a modified Darcy's law [46,81]. The specific implementations of the steady state and pressure transient methods are described in detail in our previous work [82]. For the steady-state method, shale permeability is measured when the gas flow rate becomes constant. For the transient method, it is measured when the pressure difference between the upstream and downstream reservoirs is equal to zero. In both experiments, permeability must be measured under the assumption that pressures are equalized in both the matrix and the fracture – a feature that is independent of the constraints of the two experimental methods (constant flow rate or zero difference between upstream and downstream reservoirs). According to the selection of confining pressure conditions and the gas component of the upstream reservoir, unsteady state methods can be divided into (1) Pulse decay methods, and (2) Pressure fall-off methods, including the MGE [31] and ISPP methods [61]. Among these methods, the pulse decay method is the most widely used.

To minimize the impact of different experimental conditions, we used the permeability ratio (k/k_0) to normalize the permeability evolution. For a particular experiment, a series of pressure increments/decrements was conducted under the same confining pressure. The gas pore pressure increased/decreased from the lowest/highest magnitude to the highest/lowest one. In this review based on the experimental data shown in Table 1, we used the ratio (k/k_0) of the permeability at the lowest gas pore pressure (k_0) to that at a new pressure (k) to study permeability evolution. The relations between experimental measurements of permeability evolution and applied gas pressures for CCP tests are shown in Fig. 1 with the data sources recorded in Table 1. When CO_2 was the permeant and in the supercritical phase, the permeability would decrease more significantly with injection pressure [83–86]. Thus, we excluded these measurements and only used data of CO_2 in the gaseous state.

All experimental permeability ratios distributed over a wide range (from 0.36 to 2.1) have been constrained by both lower (blue line) and upper (red line) bounds, as shown in Fig. 1(a). These data represent permeability measurements of different gases such as CO_2, CH_4, N_2, He, and Ar. The injection pressures vary between 0.2 and 15.0 MPa, whereas the confining pressures vary over the range 7.0–31.8 MPa. If we use $k/k_0 = 1$ as a further line of demarcation, the permeability ratio data can be divided into upper and the lower partitions, respectively representing net increases and decreases in terminal permeability with incremented pressure. The permeability ratio data are distributed broadly throughout the permeability-increasing and -decreasing regimes when the injected gas is either non-adsorbing (Ar and He) or weakly adsorbing (N_2), as shown in Fig. 1 (a). When the injected gas is strongly adsorbing (CH_4 and CO_2) the permeability ratio data are predominantly confined to the permeability-decrease region. These observations suggest that the gas characteristics (adsorbing or non-adsorbing) may be related to the permeability change but do not reflect a fundamental change of mechanism. The evolution of permeability for individual experiments displays a variety of curves in Fig. 1(b) from simple to complex forms, although all the tests were conducted under the same CCP conditions. Some are confined completely within the net-decrease regime whereas others occupy the net-increase regime. These observations suggest that the

Table 1
Experimental details for CCP tests.

Authors	Year	Origin	Sample size (mm)	Gas	Method	Pore Pressure (MPa)	Confining pressure (MPa)	Permeability (m^2)	Temp. (°C)	Equilibrium time	Slippage effect	r_e	b_k (MPa)	Note
Ghanizadeh et al. [32]	2014	Lower Toarcian Posidonia Shale, Northern Germany	Plugs: D: 27.20 −37.56, L: 8.17−26.70	CH_4; He	Steady state and pressure transient	0.7−3.1	12; 30	3×10^{-22}- 4.2×10^{-19}	45	24 h for stress stabilization	Y	n/a	1.2−4.2	Plugs drilled perpendicular to bedding
Guo [44]	2014	Green River formation, Pennsylvania, America	Plugs: D:25.4, L:12	He; CO_2	Pressure transient	1−5	7	3×10^{-19}-9×10^{-19}	n/a	n/a	N	n/a	n/a	/
Kang et al. [47]	2015	Longmaxi Shale, Lower Silurian marine shale gas play, China	Plugs: D:25.4, L: 38.1−50.8	CH_4; N_2	Steady state	0.3−7.6	21	1.8×10^{-18}- 2.1×10^{-17}	20	n/a	Y	less than 100 nm	0.46 for N_2, 0.71 for CH_4,	The organic-rich siliceous and carbonaceous shale samples are cored parallel to the bedding planes
Jin et al. [53]	2015	North America	Plugs: D:25.22 −25.28, L:12.21 −21.20	N_2; Ar	Pressure transient	4−9	11	2.27×10^{-18}- 1.855×10^{-17}	22	n/a	Y	n/a	n/a	Gas pressure decrease
Ren et al. [48]	2016	Qiongzhusi Formation and Longmaxi Formation of Marine Shale, Southern China	n/a	N_2	Steady state	0.15−2.55	20	1.2×10^{-18}- 7.8×10^{-18}; 3.48×10^{-17}- 4.167×10^{-16}	60	n/a	Y	n/a	0.05−0.33	Cores with well-tended appearance and cores with penetration fractures
Kumar et al. [45]	2016	Pennsylvania, America	Plugs: D:25, L:50	He; CO_2	Pressure transient	1.0−5.6	10; 15; 20	3.7×10^{-15}- 3.29×10^{-14}	n/a	n/a	N	n/a	n/a	Containing both natural and artificial fractures under nonpropped and propped conditions
Zhou et al. [30]	2016	Outcrop of the lower Silurian Longmaxi formation Changning region, Sichuan Basin, China	Plugs: D:10, L:20	N_2; He	Steady state	2−9	10	1.4×10^{-17}- 7.2×10^{-17}	35	n/a	N	n/a	n/a	Fractured by supercritical carbon dioxide
Zhu et al. [49]	2016	Longmaxi Formation, southern China	Plugs: D:25, L:50	N_2	Steady state	0.1−2	3	1.13×10^{-17}- 2.958×10^{-16}	n/a	30min	Y	n/a	n/a	/
Li et al. [43]	2017	Green River Shale, America	Plugs: D:25.4, L:50.8	CH_4; CO_2; N_2; He	Pressure transient	2−12	20	1.4×10^{-16}- 5.4×10^{-15}	21	n/a	N	n/a	n/a	Split cylindrical specimens sandwich a proppant bead-pack
Fink et al. [25]	2017	Haynesville formation (HaF); Upper Jurassic Bossier (BoM)	Plugs: D:38.0	He, Ar, N_2, CH_4, C_2H_6	Steady state; pressure transient	0.15−16 for the HaF and 0.15−12 for the BoM	8 to 20 for the HaF; 8 to 12 for the BoM	1×10^{-15}-3×10^{-15} for the HaF; 1.5×10^{-19}- 7.0×10^{-19} for the BoM	25	At least one week	Y	n/a	0.04−0.17 for the HaF and 0.14−0.71 for the BoM.	Haynesville sample plug was fractured; Bossier shale plug (BoM) was unfractured
Shen et al. [50]	2018	Barnett Shale; Eagle Ford Shale, America	Plugs: D:38.1, L:76.2	CH_4	Pressure transient	5.08−12.01	15	1.796×10^{-19}- 5.658×10^{-19}	n/a	n/a	Y	n/a	n/a	/

"Equilibrium time" represents the time interval between two consecutive permeability measurements.
"Y/N" in "slippage effect" represents whether the slippage effect was used for the explanation of shale permeability evolution. Y is yes and N is not.
"r_e" represents the radius of the mean effective flow that was explained through the Klinkenberg's model.
"b_k" represents the gas slippage factor that was explained through the Klinkenberg's model.

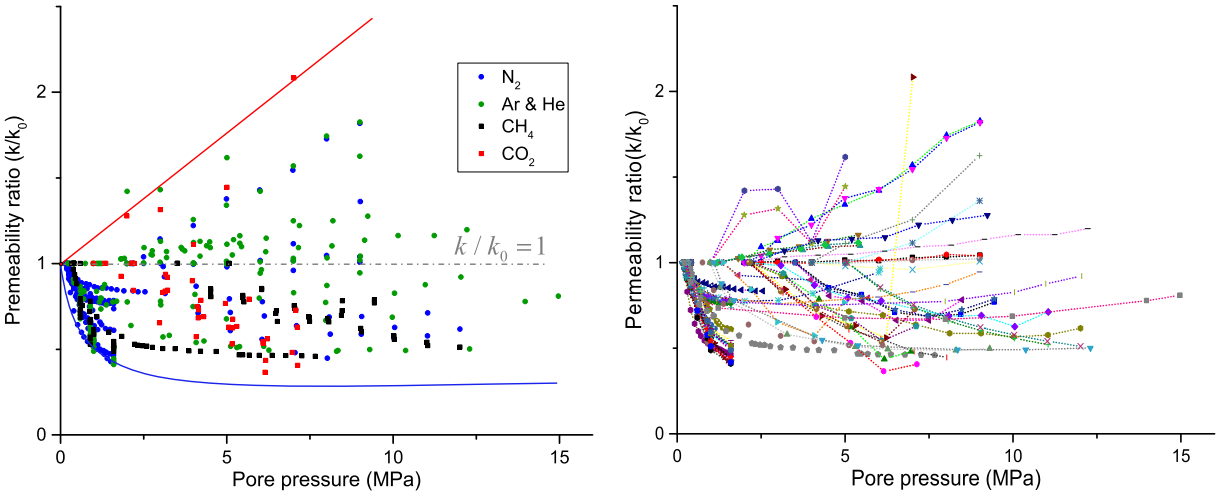

(a) Classified by gases as represented by the legend.

(b) Classified by experiments as represented by the lines.

Fig. 1. Distributions of shale experimental permeability ratios from CCP tests.

permeability evolution is not solely controlled by the external boundary conditions.

2.2. Review of constant effective stress test data

In this section, we assemble the experimental permeability data from the reported CES tests. In these experiments, the effective stress was maintained when the difference between the confining pressure and the pore pressure was kept constant for an assumed Biot's effective stress coefficient of unity. All permeabilities were evaluated under the similar assumption that pressures are equalized in both matrix and fracture.

For the CES data, we use the same method of data analysis (permeability ratio, k/k_0) as for the CCP tests. The resulting experimental measurements of the permeability ratio (k/k_0) are shown relative to gas overpressure but for constant effective stress in Fig. 2. Sources for the data are shown in Table 2.

Nearly all the permeability ratios in the CES tests are greater than zero but less than 1, as shown in Fig. 2. Similar to CCP tests, these experimental data represent a wide range of permeability measurements with different gases, including CO_2, CH_4, N_2, He, and Ar. The injection pressures varied from 0.1 to 27.6 MPa, whereas the effective stresses varied between 1.95 and 34.5 MPa within upper (red line) and lower (blue line) bounds. Most permeability ratios decrease readily with applied gas pressure for strongly adsorbing gases (CO_2 and CH_4) relative to weakly adsorbing gases (e.g. N_2) and then non-adsorbing gases (Ar and He), as shown in Fig. 2(a). This shows that, the permeability decreases more rapidly with an increase in pressure when the adsorption capacity of the injected gas is stronger. For the weakly adsorbing gas (N_2) and non-adsorbing gases (Ar and He), the rate of decrease in permeability ratio with an increase in pore pressure is spread over a wide range of permeability ratios. These observations suggest that permeability change may be related to the absorptivity of the injected gas but do

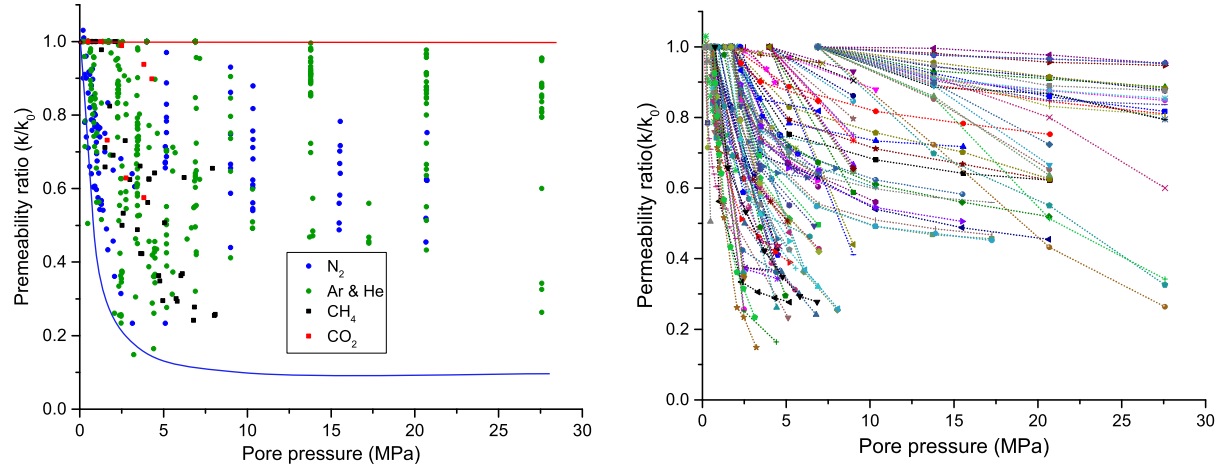

(a) Classified by gases as represented by the legend.

(b) Classified by experiments as represented by the lines.

Fig. 2. Distribution of shale experimental permeability ratios from CES tests.

Table 2
Experimental details for CES tests.

Authors	Year	Origin	Sample size (mm)	Gas	Method	Pore pressure (MPa)	Effective stress (MPa)	Permeability (m^2)	Temp. (°C)	Equilibrium time	Slippage effect	r_e	b_k (MPa)	Note
Cui et al. [61]	2010	Western Canadian Sedimentary Basin	n/a	He	Pressure transient	0.2–0.5	n/a	8.7×10^{-19}-4.46×10^{-18}	n/a	n/a	Y	n/a	0.94–1.67	/
Letham [52]	2011	Horseshoe Canyon Formation, south central Alberta	Plugs: D: 29, L: 30	CH_4; He	Pressure transient	1–8	n/a	3.8×10^{-19}-9.8×10^{-19}	n/a	n/a	Y	n/a	n/a	/
Aljamaan et al. [55]	2013	Barnett; Eagle Ford, America	Plugs: D:25, L:51	He; CO_2; CH_4; N_2	Pressure transient	0.56 –5.7; 1.00 –4.96	2.3; 3.45, 6.90, 13.79	5.3×10^{-18}-4.14×10^{-17}	n/a	n/a	Y	n/a	0.84, 6.10, 10.27 for Barnett shale; 1.05, 1.86, 2.24 for Eagle Ford shale	The Eagle Ford sample has a calcite filled fracture
Alnoaimi and Kovscek [56]	2013	Eagle Ford shale, America	Plugs: D:25, L:46	CH_4; CO_2; He	Pressure transient	0.5–5.0	3.4	1.26×10^{-17}-3.80×10^{-17}	21.5	n/a	Y	108.28 nm	1.43 for He, 1.40 for CH_4, 0.41 for CO_2	The sample has a clear calcite filled fracture that propagates in width and length
Firouzi et al. [60]	2014	Eagle Ford, America	n/a	He	Pressure transient	1.57 –2.92	3.45	4.5×10^{-14}-5.1×10^{-14}	25	n/a	Y	324.4 nm	0.48	A clear calcite filled fracture along the length of the core
Heller et al. [63]	2014	Barnett, Eagle Ford, and Marcellus, America; Montney, Canada	Plugs: L:6.9 –38.1	He	Steady state; Pressure transient	1.72 –27.59	6.9–27.6	5.0×10^{-21}-1.4×10^{-17}	45	24 h	Y	From tens of nanometers in most samples to 100–200 nm	1.35–12.49	The calcite streaks and crack are observed in three samples
Zamirian et al. [54]	2014	Marcellus Shale	Plugs: D:25.4	N_2; He	Steady state	n/a	n/a	1.26×10^{-19}-8.50×10^{-19}	n/a	n/a	Y	n/a	9.4, 35.78	/
Jin et al. [53]	2015	North America	Plugs: D:25.17 –25.36, L:7.21 –21.20	N_2; Ar	Pressure transient	4–9	2	1.825×10^{-20}-2.187×10^{-17}	22	n/a	Y	n/a	n/a	Plugs drilled parallel and perpendicular to bedding
Letham and Bustin [66]	2016	Upper Cretaceous Eagle Ford Formation, Texas, America	Plugs: D:30, L:30	He	Pressure transient	1.72 –6.89	6.89, 20.68, 34.47	3.07×10^{-21}-5.12×10^{-17}	n/a	n/a	Y	10–2059	0.08–16.44	/
Letham and Bustin [67]	2016	Montney Formation, Canada	Plug: D:30, L:30	He	Pressure transient	1.7–17.2	6.9, 20.7, 34.5, 48.3	2×10^{-16}-1.6×10^{-15}	n/a	n/a	Y	n/a	1.6–2.6	/
Moghaddam and Jamiolahmady [58]	2016	Eagle ford, Pierre and Barnett, America	Plugs: D:38.1, L:46.1, 25.4, 25.5	N_2	Steady state; Pressure transient	1.7–20.7	3.45; 6.9; 13.8; 20.7	2×10^{-17}-4.3×10^{-16}	60	n/a	Y	38-54, 16–29.1, 9–11.25 nm	2.11, 4.07, 9.01	Gas pressure decrease
Moghadam and Chalaturnyk [62]	2016	Clearwater Formation, Alberta, Canada; Montney formation,	Plugs: D:63.5, L:40; Plugs:	N_2; CH_4	Steady state	0.4–5.0; 2.0–8.0	2; 10, 20	2.8×10^{-18}-1.2×10^{-17}; 2.5×10^{-19}-2.0×10^{-18}	25	24 h	Y	n/a	8.42 for Clearwater sample; 10,710 for Montney 10D sample;	Hairline cracks were noticed on sample surfaces, and none of these seemed to go through the samples

(*continued on next page*)

Table 2 (*continued*)

Authors	Year	Origin	Sample size (mm)	Gas	Method	Pore pressure (MPa)	Effective stress (MPa)	Permeability (m^2)	Temp. (°C)	Equilibrium time	Slippage effect	r_e	b_k (MPa)	Note
		British Columbia, Canada	D:38.1, L:12										1466, 3713 for Montney 170 sample	
Peng and Loucks [31]	2016	Eagle Ford and Barnett sample, America	Plugs: D:25.4	He	Pressure transient	0.46 −0.90	6.9–37.9	8.58×10^{-20}_ 1.716×10^{-19}	22.7	24–72 h	Y	n/a	n/a	/
Zhu et al. [49]	2016	Longmaxi Formation, southern China	Plugs: D:25, L:50	N_2	Steady state	0.1–2	3	7.9×10^{-18}_ 1.03×10^{-16}	n/a	30min	Y	n/a	n/a	/
Gao and Yu [65]	2018	Carboniferous Hurleg and Huaitoutala formations, Qaidam Basin, China	Plugs: D:25, L:10.98 −12.40	He	Pressure transient	1.37 −5.51	13.79	4.65×10^{-20}_ 1.863×10^{-17}	n/a	n/a	Y	29.4–5850 nm	0.7–14.9	/
Zhao et al. [57]	2019	Longmaxi Formation, southern China	Plugs: D:50, L:100	CH_4	Pressure transient	0.5–7	5	1.39×10^{-19}_ 1.11×10^{-18}	40	12 h	Y	n/a	n/a	/

"Equilibrium time" represents the time interval between two consecutive permeability measurements.
"Y/N" in "slippage effect" represents whether the slippage effect was used for the explanation of shale permeability evolution. Y is yes and N is not.
"R_e" represents the radius of the mean effective flow that was explained through the Klinkenberg's model.
"B_k" represents the gas slippage factor that was explained through the Klinkenberg's model.

not reveal a fundamental change of mechanism. The distributions of the shale permeability ratios for individual CES tests have been shown in Fig. 2(b). Similar to the conditions for CCP measurements, the evolution of permeability for an individual experiment displays a variety of curves from simple to complex shapes for CES test. These observations suggest the same as for CCP that the permeability evolution is not solely controlled by the external boundary conditions but by intrinsic features of the sample and gas system.

3. Theoretical basis of permeability data analysis

In this section we have developed a generic permeability evolution model for shale. Based on the microstructural characteristics of shale, the permeability model is applied to delineate the boundaries of the permeability ratios as apparent in the experimental data.

3.1. Generic permeability model

The development of nanopores in shale is crucially important for gas transport. The slippage effect is believed to be one of the most important controls on the evolution of shale permeability [60,62,63,68,87]. To quantify slippage effect, a linear correlation between the apparent gas permeability (k_a) and the reciprocal of mean gas pressure (p), was proposed by Klinkenberg [68], as:

$$k_a = k_\infty \left(1 + \frac{b}{p}\right) \tag{1}$$

where k_∞ is the intrinsic permeability, p is the pore pressure, b is the gas slippage factor and is further defined as [68]:

$$b = \frac{4c\lambda p}{r_e} \tag{2}$$

where c is a proportionality factor, λ is the mean free path of the gas, and r_e is the average pore radius. The mean free path is defined as [88]:

$$\lambda = \frac{k_B T}{\sqrt{2}\pi\delta^2 p} \tag{3}$$

where k_B is the Boltzmann constant, T is the gas temperature, and $\delta$is the diameter of the gas molecule. Substituting Eqs. (2) and (3). into Eq. (1), permeability is defined as:

$$k_a = k_\infty \left(1 + \frac{2\sqrt{2}ck_B T}{\pi\delta^2 p r_e}\right) \tag{4}$$

In Klinkenberg's model, the intrinsic permeability k_∞ treated as a constant is not correlated with the stress boundary. However, the intrinsic permeability is strongly influenced by the stress condition. The intrinsic permeability k_∞ changes as a function of effective stress, therefore, the intrinsic permeability does not remain constant during the injection/depletion of shale gas extraction [42,72]. To investigate the effective stress effect, we consider absolute permeability as the intrinsic permeability. According to effective strain-based absolute permeability models [89,90], the intrinsic permeability ratio can be defined as:

$$\frac{k_\infty}{k_{\infty 0}} = \left(1 + \frac{\alpha}{\varphi_0}\Delta\varepsilon_e\right)^3 \tag{5}$$

where φ_0 and $k_{\infty 0}$ are the initial porosity and intrinsic permeability of the sample respectively at the initial effective stress $\Delta\bar{\sigma}_{e0}$, $\Delta\bar{\sigma}_{e0}$ =

$\Delta\bar{\sigma}_0 - \alpha p_0$, p_0 is the initial pore pressure with $\bar{\sigma}_0$ as the initial confining pressure, $\Delta\varepsilon_e$is defined as the total effective volumetric strain increment and α is Biot's effective stress coefficient.

Substituting Eq. (5) into Eq. (4), the apparent permeability model for shale is defined as:

$$k_a = k_{\infty 0}\left(1+\frac{\alpha}{\varphi_0}\Delta\varepsilon_e\right)^3\left(1+\frac{2\sqrt{2}ck_BT}{\pi\delta^2 p r_e}\right) \tag{6}$$

Stress-controlled boundary conditions are widely used for triaxial or hydrostatic tests. When the response is controlled by stress alone, no additional force or associated strain develops within the shale [90]. The total effective volumetric strain is defined as:

$$\Delta\varepsilon_e = -\frac{\Delta\bar{\sigma}-\Delta p}{K} \tag{7}$$

where K is the bulk modulus of the shale sample and $\bar{\sigma}$ is the mean confining stress. Then Eq. (6) can be simplified to:

$$k_a = k_{\infty 0}\underbrace{\left(1+\frac{\alpha}{\varphi_0}\frac{\Delta p-\Delta\sigma}{K}\right)^3}_{A-\text{Effective stress}}\underbrace{\left(1+\frac{2\sqrt{2}ck_BT}{\pi\delta^2 p r_e}\right)}_{B-\text{Slippage effect}} \tag{8}$$

This model shows that both terms “A-Effective stress” and “B-Slippage effect” can influence the evolution of shale apparent permeability.

3.2. Role of shale microstructure

Shale is a typical dual porosity/permeability system containing a porous matrix surrounded by fractures [91–94], as shown in Fig. 3. The “overall” permeability of the structured shale (k) is a combination of matrix permeability and fracture permeability, as:

$$k = f\left(k_m, k_f\right) \tag{9}$$

where km is matrix permeability and kf is fracture permeability.

The Knudsen number is a dimensionless number reflecting the rarefication of gas molecules and is generally used to distinguish flow regimes for gas transport [62,91], as shown in Fig. 3. The Knudsen number (K_n) is defined as the ratio of the mean free path of gas molecules (a measure of the distance between molecules) to pore size:

$$K_n = \frac{\lambda}{2r_e} \tag{10}$$

As shown in Fig. 5, the mean free path spans a broad range from 0.2 nm to 13.5 nm under different pore pressures for different kinds of gases (see input parameters for this calculation in Table 3). The mean free path decreases significantly as pore pressure is increased. So, the Knudsen number ranges from 0.001 to 0.1 [95,96] within the slip flow region, as shown in Fig. 4:

$$\frac{10k_BT}{\sqrt{2}\pi\delta^2 p} = \frac{\lambda}{0.1} \le 2r_e \le \frac{\lambda}{0.001} = \frac{1000k_BT}{\sqrt{2}\pi\delta^2 p} \tag{11}$$

The pore pressures range from 1 to 35 MPa, then for different gases, the distributions of the pore diameters ($2r_e$) subject to the slip effect are shown in Fig. 5. Thus, there is no slip-effect for flow paths greater than the micrometer-scale.

The largest pore diameters ($2r_e$) subject to slippage flow are in the range of 6.3–13.5 μm. Thus, the slippage effect needs only to be considered if the radius of the effective flow path is less than 5 μm (initial pore pressure of 1.0 MPa). Therefore, we cannot use apparent permeability theory to explain the flow in shales with effective pore radii larger than 5 μm (initial pore pressure of 1 MPa).

3.2.1. Shale with well-developed macro fractures

It is assumed that Darcy's flow occurs in the fracture system, and the gas diffuses between matrix and fracture, is controlled by the diffusion coefficient and characteristic length scale of the matrix [97,98]. When the permeability of the fracture system is much larger than that of the matrix system, the slippage effect in the matrix exerts little influence on permeability change in the fracture system. Thus, the bulk permeability of shale is a critical function of its fracture system [99–103]. Under this assumed condition, the permeability measured in experiments can be treated as the fracture permeability. Therefore, the influence of the slippage effect (B-Slippage effect) can be eliminated from Eq. (8). Then, according to Eq. (8), permeability for shale with well-developed fractures can be expressed as:

Table 3
Input parameters for mean free path calculation.

Parameter	Size
Boltzmann constant, B_k	1.38e-23 J/K
Temperature, T	303.15 K
The diameter of the gas particle (CH4),δ	0.38 nm
Proportionality factor, c	1

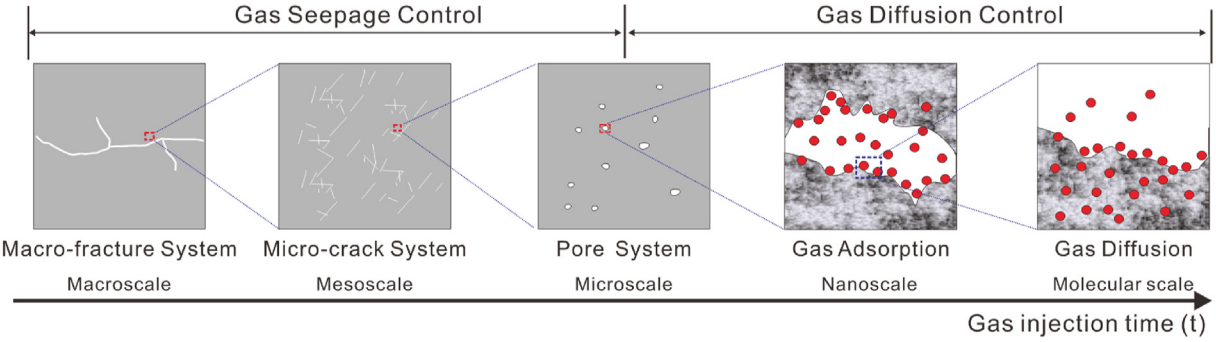

Fig. 3. Schematic representation of impacts of shale structure on the gas flow process during gas injection [91,93,94].

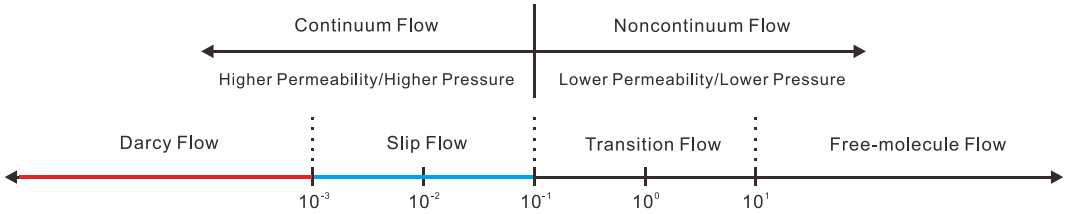

Fig. 4. Flow regimes based on Knudsen number [62,91].

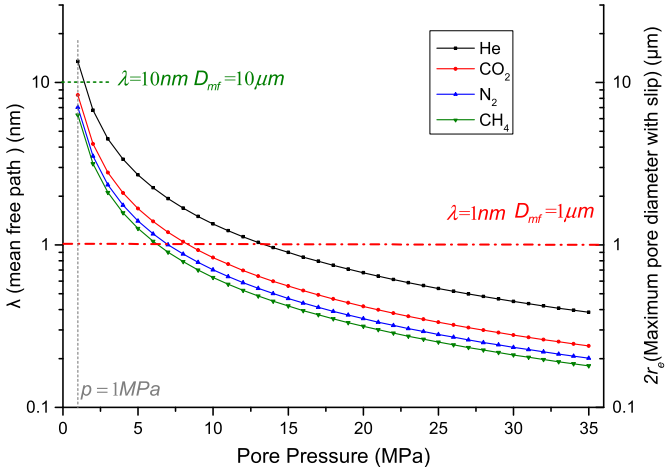

Fig. 5. Distribution of mean free path and maximum pore diameters with slippage under the influence of pore pressure.

$$k = f\left(k_m, k_f\right) \approx k_f = k_\infty = k_{\infty 0}\left(1 + \frac{\alpha}{\varphi_{f0}}\frac{\Delta p - \Delta\sigma}{K}\right)^3 \tag{12}$$

When the mean confining pressure remains unchanged (CCP), $\Delta\overline{\sigma} = 0$, Equation. (12) is simplified to:

$$\frac{k}{k_0} = \frac{k_\infty}{k_{\infty 0}} = \left(1 + \frac{\alpha}{\varphi_{f0}}\left(\frac{\Delta p}{K}\right)\right)^3 \tag{13}$$

When the effective stress remains unchanged (CES), $\Delta\overline{\sigma} - \Delta p = 0$, Equation. (12) is simplified to:

$$\frac{k}{k_0} = \frac{k_\infty}{k_{\infty 0}} = \left(1 + \frac{\alpha}{\varphi_{f0}}\left(\frac{0}{K}\right)\right)^3 = 1 \tag{14}$$

3.2.2. Shale with partially-developed macro-fractures

When the shale is devoid of macro-fractures, we consider the entire shale sample as a matrix system with the interior flow paths resulting from a connected system of micro-cracks and pores (micrometer to nanometer-scale in diameter). In this case, we consider the shale as a porous system. The permeability evolution of the shale can be influenced now by the both terms representing "A-Effective stress" and "B-Slippage effect" in Eq. (8). Therefore, the shale permeability can be expressed as:

$$k = f\left(k_m, k_f\right) \approx k_m \approx k_a = k_{\infty 0}\left(1 + \frac{\alpha}{\varphi_{m0}}\frac{\Delta p - \Delta\sigma}{K}\right)^3\left(1 + \frac{2\sqrt{2}ck_BT}{\pi\delta^2 pr_e}\right) \tag{15}$$

When the confining pressure remains unchanged (CCP), $\Delta\overline{\sigma} = 0$, and Eq. (15) is simplified to:

$$\frac{k}{k_0} = \frac{k_a}{k_{a0}} = \frac{\left(1 + \frac{\alpha}{\varphi_{m0}}\frac{\Delta p}{K}\right)^3\left(1 + \frac{2\sqrt{2}ck_BT}{\pi\delta^2 pr_e}\right)}{1 + \frac{2\sqrt{2}ck_BT}{\pi\delta^2 p_0 r_e}} \tag{16}$$

When the effective stress remains unchanged (CES), $\Delta\overline{\sigma} - \Delta p = 0$, and Eq. (15) is simplified to:

$$\frac{k}{k_0} = \frac{k_a}{k_{a0}} = \frac{1 + \frac{2\sqrt{2}ck_BT}{\pi\delta^2 pr_e}}{1 + \frac{2\sqrt{2}ck_BT}{\pi\delta^2 p_0 r_e}} \tag{17}$$

3.3. Delineation of permeability regime boundaries under CCP conditions

Equation.(13) can be used to calculate the intrinsic permeability ratios, $k_\infty/k_{\infty 0}$, for shale with well-developed macro-fractures (fractured shale) under CCP conditions, and the Eq. (16) to calculate the apparent permeability ratio, k_a/k_{a0}, for shale with less-developed fractures (shale matrix). These results are shown in Fig. 6. The input parameters for the calculations are reported in Table 3.

The permeability ratios are confined between upper and lower bounds, as shown in Fig. 6. The upper bound represents the behavior of shale with well-developed fractures, as defined by Eq. (13), whereas the lower bound represents behavior without natural fractures, as defined by Eq. (16). In this illustration (Fig. 6), we use a smaller porosity and bulk modulus to represent the shale with well-developed fractures:$\varphi_{f0} = 0.01$ and $K = 2.7GPa$. These magnitudes are substituted into Eq. (13) to show the permeability upper bound. The transition from upper to lower bound corresponds to the magnitude of pore size from macroscale to nanoscale. When the mean effective flow path is sufficiently large, the slippage effect can be neglected. We assume this situation as the demarcation between flow regimes. For illustration, we assume $\varphi_{m0} = 0.05$ and $K = 27GPa$ as demarcation, and use Eq. (13) to define this critical boundary (red short dash-dotted line in Fig. 6). Below this demarcation line, the slippage effect becomes more significant as the pore size decreases whereas the effective stress effect becomes less significant. For intact shale without fractures, the permeability ratio corresponds to the lower bound of permeability ratios. The lower bounds are dependent on the magnitudes of matrix pore sizes, as shown in Fig. 6. For example, $r_e = 0.5\mu m$ and $r_e = 50nm$ correspond to two lower bounds.

In the upper zone, the bulk modulus (K) of the shale sample with less-developed macro-fractures is much larger than that of the fractured shales [104,105]. It is assumed that

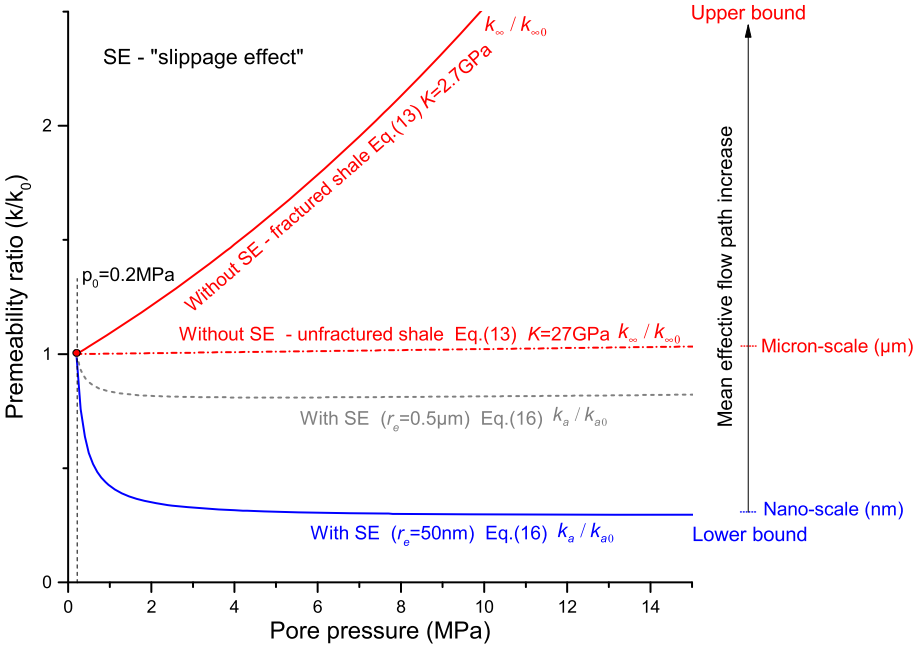

Fig. 6. Example analytical solutions for permeability ratios under CCP conditions.

$\varphi_{f0} = 0.01$, $K = 2.7GPa$ for the shale samples with well-developed macro fractures (fractured shale) represent the upper bound. From the demarcation line (without SE - unfractured shale) representing the upper bound (without SE - fractured shale) the evolution of shale permeability is influenced by the decrease in the bulk modulus (K) of the shale sample. The permeability of sample increases directly with an increase in pore pressure without the influence of the slippage effect under this condition. The behaviors of "real" shales are typically distributed between these lower and upper bounds, representing typical dual/multiple porous systems. Thus, their behaviors are highly dependent on the multiple interactions between pore systems.

3.4. Delineation of permeability boundaries under CES conditions

Equations.(14) and (17) can also be used to calculate permeability ratios under constant effective stress (CES) conditions. The input parameters for the calculation are defined in Table 3. The range for this variation in permeability ratio corresponds to the magnitude of the mean effective flow path shown in Fig. 7. In these calculations, the bulk modulus (K) of the shale exerts no influence on shale permeability because the effective stress is maintained constant.

The permeability ratios have been remained less than unity (upper bound) under CES conditions, as shown in Fig. 7 (solid red curve). This represents the case of shale with well-developed

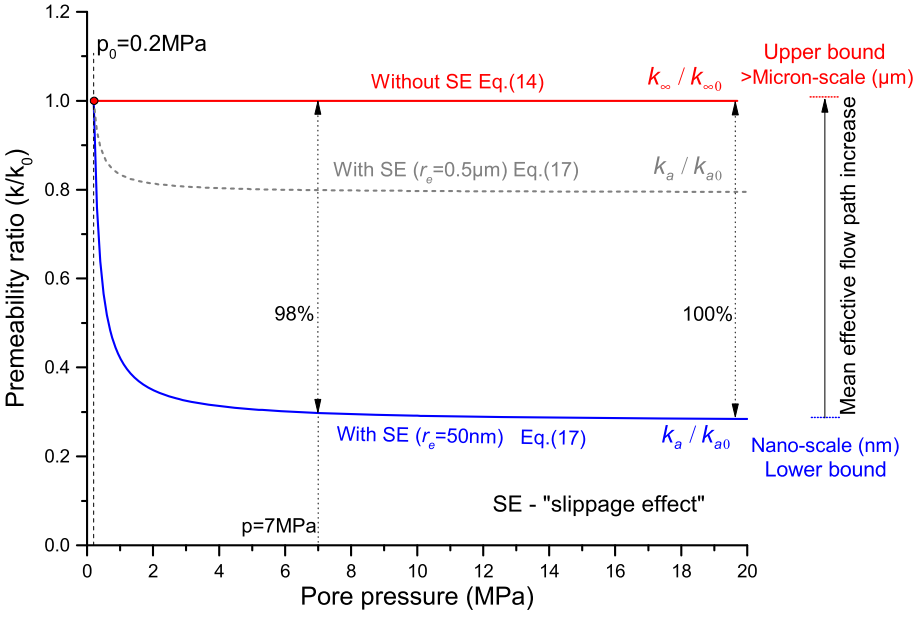

Fig. 7. Example of analytical solutions for evolution of permeability ratios under CES conditions.

macro-fractures, and under this condition, the slippage effect can be ignored. As the mean effective flow path decreases, the role of slippage effect increases. At nanometer-scale, the slippage effect dominates response and delineates the lower bound to the permeability ratios as shown by the solid blue line in Fig. 7. This line is dependent on the magnitude of the effective flow path given by Eq. (17). The magnitude of the mean effective flow path changes to $0.5\mu m$, then the lower bound moves to the dotted line.

When pore pressures increase to 7 MPa ($p_0 = 0.2$ MPa) the permeability ratio has been reduced by fully 98% of the overall total decline. Thus, the slippage effect contributes a significant decrease in shale permeability for the modest increases in pore pressure, but this only occurs in the low pore pressure regime. Thus the influence of the gas slippage effect on shale permeability need only be considered at low gas pressures (<7 MPa) [67].

4. Analysis of experimental permeability data

The broad array of experimental data collected from CCP and CES tests have been compared with these theoretically-delineated regimes of permeability evolution. This comparison allows significant mechanism-based insights to elucidate the role of shale microstructure on the evolution of permeability.

The comparisons between theoretical solutions and experimental observations under CCP conditions are shown in Fig. 8 (a). We assume that $\varphi_{f0} = 0.01, K = 2.7GPa$, then according to Eq. (13), the upper bound to the permeability evolution data can be defined. The collected experimental results of the previous studies [30,43] also show that the permeability data from the fractured shale samples are also distributed near this boundary. On the other side, if we assume that $\varphi_{m0} = 0.05$, $K = 27GPa$, $p_0 = 0.2MPa$, $r_e = 60nm$, then according to Eq. (16), the lower bound to the permeability evolution data can be demarcated as well. Fig. 8 (b) shows the comparison of the permeability evoloution data under CES conditions.

As apparent in Fig. 8(a) and (b), all permeability data are indeed confined within the regime boundaries defined by our analyses. This outcome suggests that the actual shales used in these experiments are transitional between cases with well-developed macro-fractures and intact shale absent macro-fractures. Therefore, when we analyze the data and their distribution, we must treat all shale samples as the representative of multiple porosity systems. For shales with multi-scale pore systems, the interactions among multiple processes triggered by gas injection/depletion exert a dominant impact on the distribution of shale permeability evolution ratios.

For example, the distribution of permeability ratios is strongly related to gas compositionin both CCP and CES tests (Fig. 8). Permeability ratios decrease more rapidly with the increase in pressure for strongly adsorbing gases (CO_2 and CH_4) than for weakly adsorbing gases (N_2) and non-adsorbing gases (Ar and He). The theoretical solutions are derived for the ultimate equilibrium condition, i.e., pressures in both matrix and fracture are equal. All permeability measurements were also conducted under the same assumption. If all such assumptions are true, then the given results should be similar. However, any discrepancies suggest that the shale samples have not yet reached pressure equilibrium during the test. This phenomenon has been observed in recent laboratory experiments [103,106,107] and numerical models [23,73,76,80]. According to these latest studies, the evolution of permeability under the influence of interaction between matrix and fractures can be divided into three distinct stages [82,107,108] as successive stages of permeability decrease, then rebound and followed by ultimate stabilization. The stage of permeability decrease occurs

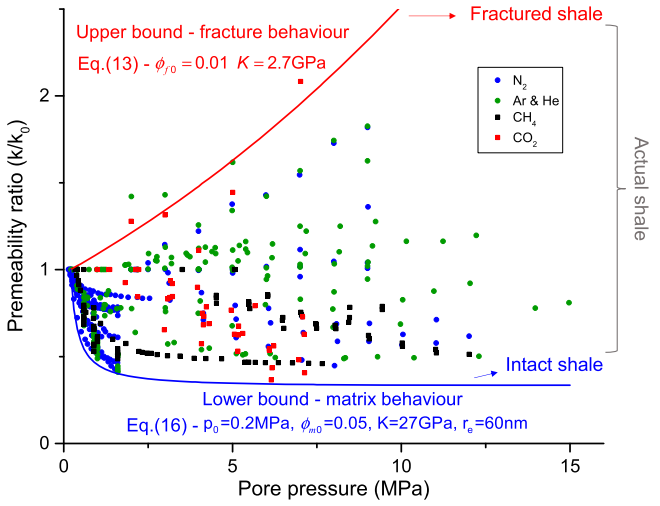

(a) Distribution among permeability evolution bounds for CCP behavior.

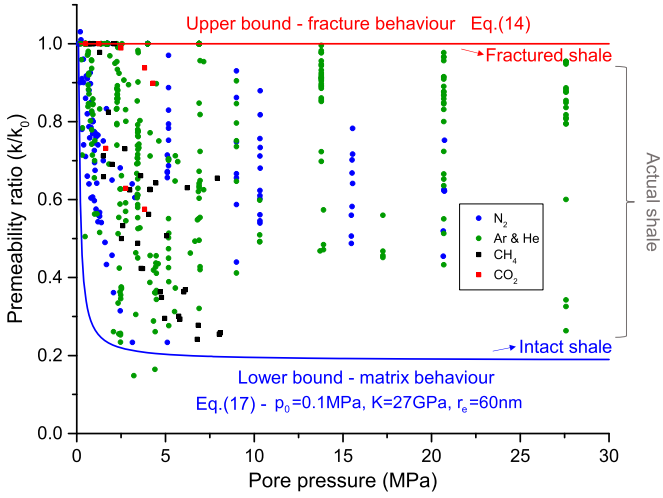

(b) Distribution among permeability evolution bounds for CES behavior.

Fig. 8. Comparison between theoretical solutions and experimental observation.

immediately after gas injection when the gas has rapidly invaded the fracture due to its relatively high permeability and begins to diffuse into the fracture wall. Under this condition, the matrix near the fracture swells, causing the fracture to narrow and this results in the permeability decrease. The next stage is rebound (permeability increase). As gas diffusion into the matrix at the fracture wall continues, the swelling zone widens and the fracture reopens - leading to permeability rebound. During final stabilization, a new equilibrium state between the fracture and the matrix is attained, and the permeability remains unchanged. These stages represent the evolution of shale permeability from initial to ultimate equilibrium. The regime behaviors discussed in this paper represent that the permeability ratio follows stabilization to the initial permeability - while the contributing experimental measurements may represent permeability ratios anywhere in this transition from initial (unchanged) to ultimate (pressure-stabilized) permeability.

5. Conclusions

This study provides a mechanism-based study of experimental observations of shale permeability evolution under constraints of both constant confining pressure (CCP) and constant effective

stress (CES) conditions. Based on these critical analyses, the following conclusions can be drawn:

(1) The permeability ratios in the shale permeability tests are represented by an upper bound that is controlled by the fracture response, and a lower bound is defined by matrix behavior. The evolution of shale permeability in upper bound is controlled primarily by the impact of effective stress in the fracture network, whereas for the lower bound it is controlled by both the effective stress effect and the gas slippage effect in the matrix.
(2) Evolution in permeability within the region intermediate to these upper and lower bounds is modulated by both the characteristics of the multiscale pore architecture and physical processes acting across different scales. All evolutions of permeability ratios with gas pressure display a variety of curves, from simple to complex, but all are limited to being within the region.
(3) A first order analysis of permeability changes within the region concludes that the relative importance of effective stress and slippage effects is regulated by the multiscale structural characteristics of the pore architecture and the interactions of multiple processes across different scales.
(4) This review of outcomes, as presented, suggests that the factors, including effective stress, gas sorption and slippage can be separated through current CCP and CES tests only for idealized shales. For shale samples with well-developed fractures, the shale behaviors are dominated by the fracture behavior. This defines the upper bound. On the other side, for shale samples without fractures, the shale behaviors are dominated by the matrix behavior. This defines the lower bound. For actual shales, their behaviors are regulated by their internal multiscale pore structural characteristics and the interactions of multiple processes across different scales. Thus, internal dependencies of effective stress, gas sorption and slippage cannot be fully understood through the nature of the external boundary conditions (CCP and CES), alone, but require high-level knowledge of sample structure and process interactions. This situation is exacerbated by the observation that these interactions endure for an extended period – possibly lasting years – complicating the interpretation of laboratory experiments and prediction of field behavior.
(5) The long-lasting nature of process interactions within shale samples is believed as the true reason why current experimental measurements of shale permeability are not consistent with predictions of commonly-used permeability models. Based on this reason, the nature of permeability time dependencies on the internal process interactions must be reflected in any future experimental and modeling research.

Credit author statement

Rui Shi: Writing – original draft, Methodology, Investigation, Validation. Jishan Liu: Conceptualization, Writing- Reviewing and Editing. Xiaoming Wang: Resources, Methodology, Supervision. Mingyao Wei: Methodology. Derek Elsworth: Conceptualization, Writing- Reviewing and Editing.

Declaration of competing interest

The authors declare that they have no known competing financial interests or personal relationships that could have appeared to influence the work reported in this paper.

Acknowledgements

This work was funded by the National Key R&D Program of China (2020YFA0711800), the Natural Science Foundation of China(41972184), Shanxi science and technology plan announced bidding project (20201101002), the Fund of Outstanding Talents in Discipline of China University of Geosciences (Wuhan) (102−162301192664), and the PetroChina Innovation Foundation(2019D-5007-0107). These various sources of support are gratefully acknowledged.

Appendix A. Supplementary data

Supplementary data to this article can be found online at https://doi.org/10.1016/j.energy.2021.121405.

References

[1] Aydin G. Regression models for forecasting global oil production. Petrol Sci Technol 2015;33(21−22):1822−8.
[2] Aydin G, Jang H, Topal E. Energy consumption modeling using artificial neural networks: the case of the world's highest consumers. Energy Sources B Energy Econ Plann 2016;11(3):212−9.
[3] Feng Y, Zhang L. Scenario analysis of urban energy saving and carbon abatement policies: a case study of Beijing city, China. Procedia Environmental Sciences 2012;13:632−44.
[4] Karacan CÖ, Ruiz FA, Cotè M, Phipps S. Coal mine methane: a review of capture and utilization practices with benefits to mining safety and to greenhouse gas reduction. Int J Coal Geol 2011;86(2−3):121−56.
[5] Mistré M, Crénes M, Hafner M. Shale gas production costs: historical developments and outlook. Energy strategy reviews 2018;20:20−5.
[6] EIA. Annual energy Outlook 2017 with Projections to 2040. Office of Scientific & Technical Information Technical Reports; 2017.
[7] Ma L, Dowey PJ, Rutter E, Taylor KG, Lee PD. A novel upscaling procedure for characterising heterogeneous shale porosity from nanometer-to millimetre-scale in 3D. Energy 2019;181:1285−97.
[8] An C, Killough J, Mi L. Stress-dependent permeability of organic-rich shale reservoirs: impacts of stress changes and matrix shrinkage. J Petrol Sci Eng 2019;172:1034−47.
[9] Liu Y, Yao Y, Liu D, Zheng S, Sun G, Chang Y. Shale pore size classification: an NMR fluid typing method. Mar Petrol Geol 2018;96:591−601.
[10] Loucks RG, Reed RM, Ruppel SC, Jarvie DM. Morphology, genesis, and distribution of nanometer-scale pores in siliceous mudstones of the Mississippian Barnett Shale. J Sediment Res 2009;79(12):848−61.
[11] Curtis ME, Ambrose RJ, Sondergeld CH. Structural characterization of gas shales on the micro-and nano-scales. Conference Structural characterization of gas shales on the micro-and nano-scales. Society of Petroleum Engineers; 2010.
[12] Rutter E, Mecklenburgh J, Taylor K. Geomechanical and petrophysical properties of mudrocks: introduction454. Geological Society, London, Special Publications; 2017. p. 1−13. 1.
[13] Sondergeld CH, Ambrose RJ, Rai CS, Moncrieff J. Micro-structural studies of gas shales. Conference Micro-structural studies of gas shales. Society of Petroleum Engineers; 2010.
[14] Wang FP, Reed RM. Pore networks and fluid flow in gas shales. Conference Pore networks and fluid flow in gas shales. Society of Petroleum Engineers; 2009.
[15] Wan Y, Pan Z, Tang S, Connell LD, Down DD, Camilleri M. An experimental investigation of diffusivity and porosity anisotropy of a Chinese gas shale. J Nat Gas Sci Eng 2015;23:70−9.
[16] Liu S, Zhang R, Karpyn Z, Yoon H, Dewers T. Investigation of accessible pore structure evolution under pressurization and adsorption for coal and shale using small-angle neutron scattering. Energy Fuels 2019;33(2):837−47.
[17] Sang G, Liu S, Zhang R, Elsworth D, He L. Nanopore characterization of mine roof shales by SANS, nitrogen adsorption, and mercury intrusion: impact on water adsorption/retention behavior. Int J Coal Geol 2018;200:173−85.
[18] Ougier-Simonin A, Renard F, Boehm C, Vidal-Gilbert S. Microfracturing and microporosity in shales. Earth Sci Rev 2016;162:198−226.
[19] Chen T, Feng XT, Pan Z. Experimental study of swelling of organic rich shale in methane. Int J Coal Geol 2015;150−151:64−73.
[20] Cui G, Liu J, Wei M, Feng X, Elsworth D. Evolution of permeability during the process of shale gas extraction. J Nat Gas Sci Eng 2018;49:94−109.
[21] Yao Y, Liu J, Liu D, Chen J, Pan Z. A new application of NMR in characterization of multiphase methane and adsorption capacity of shale. Int J Coal Geol 2019;201:76−85.
[22] Karacan CÖ. Swelling-induced volumetric strains internal to a stressed coal associated with CO2 sorption. Int J Coal Geol 2007;72(3−4):209−20.
[23] Cui G, Feng X-T, Pan Z, Chen T, Liu J, Elsworth D, et al. Impact of shale matrix mechanical interactions on gas transport during production. J Petrol Sci Eng

2020;184:106524.
[24] Tan Y, Pan Z, Feng X-T, Zhang D, Connell LD, Li S. Laboratory characterisation of fracture compressibility for coal and shale gas reservoir rocks: a review. Int J Coal Geol 2019;204:1–17.
[25] Fink R, Krooss BM, Gensterblum Y, Amann-Hildenbrand A. Apparent permeability of gas shales–Superposition of fluid-dynamic and poro-elastic effects. Fuel 2017;199:532–50.
[26] Fink R, Letham E, Krooss B, Amann-Hildenbrand A. Caution when comparing simulation results and experimental shale permeability data: reply to" Comments on" Apparent permeability of gas shales-Superposition of fluid-dynamic and poro-elastic effects" by Fink et al." by Moghaddam 2018;234:1545–9. Fuel.
[27] Moghaddam RN. Comments on" Apparent permeability of gas shales-Superposition of fluid-dynamic and poro-elastic effects" by Fink et al. Fuel 2018;234:1541–4.
[28] Chen T, Feng X-T, Cui G, Tan Y, Pan Z. Experimental study of permeability change of organic-rich gas shales under high effective stress. J Nat Gas Sci Eng 2019;64:1–14.
[29] Pan Z, Ma Y, Danesh NN, Connell LD, Sander R, Down DI, et al. Measurement of shale anisotropic permeability and its impact on shale gas production. Conference Measurement of shale anisotropic permeability and its impact on shale gas production. Society of Petroleum Engineers; 2015.
[30] Zhou J, Liu G, Jiang Y, Xian X, Liu Q, Zhang D, et al. Supercritical carbon dioxide fracturing in shale and the coupled effects on the permeability of fractured shale: an experimental study. J Nat Gas Sci Eng 2016;36:369–77.
[31] Peng S, Loucks B. Permeability measurements in mudrocks using gas-expansion methods on plug and crushed-rock samples. Mar Petrol Geol 2016;73:299–310.
[32] Ghanizadeh A, Amann-Hildenbrand A, Gasparik M, Gensterblum Y, Krooss BM, Littke R. Experimental study of fluid transport processes in the matrix system of the European organic-rich shales: II. Posidonia Shale (Lower Toarcian, northern Germany). Int J Coal Geol 2014;123:20–33.
[33] Zamirian M, Aminian KK, Ameri S, Fathi E. New steady-state technique for measuring shale core plug permeability. Conference New steady-state technique for measuring shale core plug permeability. Society of Petroleum Engineers; 2014.
[34] Tan Y, Pan Z, Liu J, Feng X-T, Connell LD. Laboratory study of proppant on shale fracture permeability and compressibility. Fuel 2018;222:83–97.
[35] Tan Y, Pan Z, Liu J, Wu Y, Haque A, Connell LD. Experimental study of permeability and its anisotropy for shale fracture supported with proppant. J Nat Gas Sci Eng 2017;44:250–64.
[36] Zhou J, Zhang L, Li X, Pan Z. Experimental and modeling study of the stress-dependent permeability of a single fracture in shale under high effective stress. Fuel 2019;257:116078.
[37] Wang X, Zhu Y, Fu C. Experimental investigation of the stress-dependent permeability in the Longmaxi Formation shale. J Petrol Sci Eng 2019;175:932–47.
[38] Chen Y, Jiang C, Yin G, Wojtanowicz AK, Zhang D. Permeability and effective stress in dipping gas shale formation with bedding—experimental study. J Energy Resour Technol 2020;142(10).
[39] McKernan R, Rutter E, Mecklenburgh J, Taylor K, Covey-Crump S. Influence of effective pressure on mudstone matrix permeability: implications for shale gas production. Conference Influence of effective pressure on mudstone matrix permeability: implications for shale gas production, vol. 2014. European Association of Geoscientists & Engineers; 2014. p. 1–13.
[40] Ma Y, Pan Z, Zhong N, Connell LD, Down DI, Lin W, et al. Experimental study of anisotropic gas permeability and its relationship with fracture structure of Longmaxi Shales, Sichuan Basin, China. Fuel 2016;180:106–15.
[41] Van Noort R, Yarushina V. Water, CO 2 and argon permeabilities of intact and fractured shale cores under stress. Rock Mech Rock Eng 2019;52(2):299–319.
[42] Pan Z, Ma Y, Danesh NN, Connell LD, Sander R, Down DI, et al. Measurement of shale anisotropic permeability and its impact on shale gas production. In: Conference Measurement of shale anisotropic permeability and its impact on shale gas production, Brisbane, Australia; 2015. p. 1–15.
[43] Li X, Feng Z, Han G, Elsworth D, Marone C, Saffer D, et al. Permeability evolution of propped artificial fractures in green river shale. Rock Mech Rock Eng 2017;50(6):1473–85.
[44] Guo F. Experimental investigation of shale permeability. The University of Western Australia; 2014.
[45] Kumar H, Elsworth D, Mathews J, Marone C. Permeability evolution in sorbing media: analogies between organic-rich shale and coal. Geofluids 2016;16(1):43–55.
[46] Sander R, Pan Z, Connell LD. Laboratory measurement of low permeability unconventional gas reservoir rocks: a review of experimental methods. J Nat Gas Sci Eng 2017;37:248–79.
[47] Kang Y, Chen M, Li X, You L, Yang B. Laboratory measurement and interpretation of nonlinear gas flow in shale. Int J Mod Phys C 2015;26(6):1550063.
[48] Ren Y, Guo X, Xie C, Wu H. Experimental study on gas slippage of marine shale in southern China. Petroleum 2016;2(2):171–6.
[49] Zhu W, Tian W, Gao Y, Deng J, Zhang X, Qi Q, et al. Study on experiment conditions of marine shale gas seepage law. Journal of Natural Gas Geoscience 2016;1(2):157–63.
[50] Shen Y, Pang Y, Shen Z, Tian Y, Ge H. Multiparameter analysis of gas transport phenomena in shale gas reservoirs: apparent permeability characterization. Sci Rep 2018;8(1):2601.
[51] Wu T, Pan Z, Connell LD, Camilleri M, Fu X. Apparent gas permeability behaviour in the near critical region for real gases. J Nat Gas Sci Eng 2020:103245.
[52] Letham EA. Matrix permeability measurements of gas shales: gas slippage and adsorption as sources of Systematic Error. 2011.
[53] Jin G, Pérez HG, Agrawal G, Khodja MR, Ali AZ, Hussaini SR, et al. The impact of gas adsorption and composition on unconventional shale permeability measurement. In: Conference the impact of gas adsorption and composition on unconventional shale permeability measurement, Manama, Bahrain; 2015. p. 1–13.
[54] Zamirian M, Aminian KK, Ameri S, Fathi E. New steady-state technique for measuring shale core plug permeability. Conference New steady-state technique for measuring shale core plug permeability. Calgary, Alberta: Canada; 2014. p. 1–11.
[55] Aljamaan H, Alnoaimi K, Kovscek A. In-depth experimental investigation of shale physical and transport properties. In: Unconventional Resources Technology Conference. Denver, Colorado; 2013. p. 1120–9.
[56] Alnoaimi K, Kovscek A. Experimental and numerical analysis of gas transport in shale including the role of sorption. SPE Annual Technical Conference and Exhibition. New Orleans: Louisiana; 2013. p. 1–16. USA.
[57] Zhao Y, Wang C, Zhang Y, Liu Q. Experimental study of adsorption effects on shale permeability. Nat Resour Res 2019;28(4):1575–86.
[58] Moghaddam RN, Jamiolahmady M. Fluid transport in shale gas reservoirs: simultaneous effects of stress and slippage on matrix permeability. Int J Coal Geol 2016;163:87–99.
[59] Moghadam AA, Chalaturnyk R. Laboratory investigation of shale permeability. In: Conference laboratory investigation of shale permeability, Calgary, Alberta, Canada; 2015. p. 1–27.
[60] Firouzi M, Alnoaimi K, Kovscek A, Wilcox J. Klinkenberg effect on predicting and measuring helium permeability in gas shales. Int J Coal Geol 2014;123:62–8.
[61] Cui XA, Bustin RM, Brezovski R, Nassichuk B, Glover K, Pathi V. A new method to simultaneously measure in-situ permeability and porosity under reservoir conditions: implications for characterization of unconventional gas reservoirs. Conference A new method to simultaneously measure in-situ permeability and porosity under reservoir conditions: Implications for characterization of unconventional gas reservoirs. Calgary, Alberta: Canada; 2010. p. 1–8.
[62] Moghadam AA, Chalaturnyk R. Analytical and experimental investigations of gas-flow regimes in shales considering the influence of mean effective stress. SPE J 2016;21(2):557–72.
[63] Heller R, Vermylen J, Zoback M. Experimental investigation of matrix permeability of gas shales. AAPG Bull 2014;98(5):975–95.
[64] Alnoaimi KR, Duchateau C, Kovscek A. Characterization and measurement of multi-scale gas transport in shale core samples. In: Conference Characterization and measurement of multi-scale gas transport in shale core samples, Denver, Colorado, USA; 2014. p. 1–19.
[65] Gao J, Yu Q. Effect of water saturation on pressure-dependent permeability of carboniferous shale of the qaidam basin, China123. Transp Porous Media; 2018. p. 147–72. 1.
[66] Letham EA, Bustin RM. Klinkenberg gas slippage measurements as a means for shale pore structure characterization. Geofluids 2016;16(2):264–78.
[67] Letham EA, Bustin RM. The impact of gas slippage on permeability effective stress laws: implications for predicting permeability of fine-grained lithologies. Int J Coal Geol 2016;167:93–102.
[68] Klinkenberg L. The permeability of porous media to liquids and gases. In: Conference the permeability of porous media to liquids and gases, New York, USA; 1941. p. 200–13.
[69] Florence FA, Rushing J, Newsham KE, Blasingame TA. Improved permeability prediction relations for low permeability sands. In: Conference Improved permeability prediction relations for low permeability sands, Denver, Colorado, USA; 2007. p. 1–18.
[70] Wang D, Yao J, Chen Z, Song W, Sun H. Image-based core-scale real gas apparent permeability from pore-scale experimental data in shale reservoirs. Fuel 2019;254:115596.
[71] Sheng G, Javadpour F, Su Y. Dynamic porosity and apparent permeability in porous organic matter of shale gas reservoirs. Fuel 2019;251:341–51.
[72] Wei M, Liu J, Feng X, Wang C, Zhou F. Evolution of shale apparent permeability from stress-controlled to displacement-controlled conditions. J Nat Gas Sci Eng 2016;34:1453–60.
[73] Wei M, Liu Y, Liu J, Elsworth D, Zhou F. Micro-scale investigation on coupling of gas diffusion and mechanical deformation of shale. J Petrol Sci Eng 2019;175:961–70.
[74] Zeng J, Liu J, Li W, Leong Y-K, Elsworth D, Guo J. Evolution of shale permeability under the influence of gas diffusion from the fracture wall into the matrix. Energy Fuels 2020;34(4):4393–406.
[75] Li W, Liu J, Zeng J, Leong Y-K, Elsworth D, Tian J, et al. A fully coupled multidomain and multiphysics model for evaluation of shale gas extraction. Fuel 2020;278:118214.
[76] Cui G, Liu J, Wei M, Shi R, Elsworth D. Why shale permeability changes under variable effective stresses: new insights. Fuel 2018;213:55–71.
[77] Shi R, Liu J, Elsworth D. Mechanistic analysis of shale permeability evolution data. Conference Mechanistic analysis of shale permeability evolution data.

Unconventional Resources Technology Conference (URTEC); 2019.
[78] Liu X, Sheng J, Liu J, Hu Y. Evolution of coal permeability during gas injection—from initial to ultimate equilibrium. Energies 2018;11(10):2800.
[79] Wang C, Zhai P, Chen Z, Liu J, Wang L, Xie J. Experimental study of coal matrix-cleat interaction under constant volume boundary condition. Int J Coal Geol 2017;181:124–32.
[80] Zeng J, Liu J, Li W, Tian J, Leong Y-K, Elsworth D, et al. Effects of heterogeneous local swelling on coal and shale permeability evolution. Conference effects of Heterogeneous Local swelling on coal and shale permeability evolution, vol. 2020. European Association of Geoscientists & Engineers; 2020. p. 1–27.
[81] Huang Q, Liu S, Cheng W, Wang G. Fracture permeability damage and recovery behaviors with fracturing fluid treatment of coal: an experimental study. Fuel 2020;282:118809.
[82] Shi R, Liu J, Wei M, Elsworth D, Wang X. Mechanistic analysis of coal permeability evolution data under stress-controlled conditions. Int J Rock Mech Min Sci 2018;110:36–47.
[83] Ranathunga A, Perera M, Ranjith P, De Silva G. A macro-scale view of the influence of effective stress on carbon dioxide flow behaviour in coal: an experimental study. Geomechanics and Geophysics for Geo-Energy and Geo-Resources 2017;3(1):13–28.
[84] Zhang X, Ranjith P, Perera M, Ranathunga A, Haque A. Gas transportation and enhanced coalbed methane recovery processes in deep coal seams: a review. Energy Fuels 2016;30(11):8832–49.
[85] Jia W, McPherson B, Dai Z, Irons T, Xiao T. Evaluation of pressure management strategies and impact of simplifications for a post-EOR CO2 storage project. Geomechanics and Geophysics for Geo-Energy and Geo-Resources 2017;3(3):281–92.
[86] Zhou J, Tian S, Zhou L, Xian X, Yang K, Jiang Y, et al. Experimental investigation on the influence of sub-and super-critical CO2 saturation time on the permeability of fractured shale. Energy 2020;191:116574.
[87] Liu A, Wang K, Zang J, Du F, Zhou A. Relative permeability of gas for unconventional reservoirs124. Transp Porous Media; 2018. p. 289–307. 1.
[88] Loeb BLB. The kinetic theory of gases. Methuen; 1934.
[89] Liu J, Chen Z, Elsworth D, Miao X, Mao X. Evolution of coal permeability from stress-controlled to displacement-controlled swelling conditions. Fuel 2011;90(10):2987–97.
[90] Liu J, Chen Z, Elsworth D, Qu H, Chen D. Interactions of multiple processes during CBM extraction: a critical review. Int J Coal Geol 2011;87(3):175–89.
[91] Javadpour F, Fisher D, Unsworth M. Nanoscale gas flow in shale gas sediments. J Can Petrol Technol 2007;46(10).
[92] Dewhurst DN, Siggins AF. Impact of fabric, microcracks and stress field on shale anisotropy. Geophys J Int 2006;165(1):135–48.
[93] Loucks RG, Reed RM, Ruppel SC, Hammes U. Spectrum of pore types and networks in mudrocks and a descriptive classification for matrix-related mudrock pores. AAPG Bull 2012;96(6):1071–98.
[94] Chen S, Han Y, Fu C, Zhu Y, Zuo Z. Micro and nano-size pores of clay minerals in shale reservoirs: implication for the accumulation of shale gas. Sediment Geol 2016;342:180–90.
[95] Hadjiconstantinou NG. The limits of Navier-Stokes theory and kinetic extensions for describing small-scale gaseous hydrodynamics. Phys Fluids 2006;18(11):111301.
[96] Yuan Y, Rahman S. Extended application of lattice Boltzmann method to rarefied gas flow in micro-channels. Physica A Statistical Mechanics & Its Applications 2016;463:25–36.
[97] Purl R, Evanoff J, Brugler M. Measurement of coal cleat porosity and relative permeability characteristics. In: SPE gas technology Symposium. Houston; 1991.
[98] Liu A, Liu S, Hou X, Liu P. Transient gas diffusivity evaluation and modeling for methane and helium in coal. Int J Heat Mass Tran 2020;159:120091.
[99] Palmer I. Permeability changes in coal: analytical modeling. Int J Coal Geol 2009;77(1):119–26.
[100] Ried G, Towler B, Harris H. Simulation and economics of coalbed methane production in the Powder River Basin. SPE Rocky Mountain Regional Meeting; 1992. p. 425–32. Casper.
[101] Sparks D, McLendon T, Saulsberry J, Lambert S. The effects of stress on coalbed reservoir performance, Black Warrior Basin, USA. Conference the effects of stress on coalbed reservoir performance. USA, Dallas: Black Warrior Basin; 1995. p. 339–51.
[102] Pan Z, Connell LD. Modelling permeability for coal reservoirs: a review of analytical models and testing data. Int J Coal Geol 2012;92:1–44.
[103] Shi R, Liu J, Wang X, Elsworth D, Liu Z, Wei M, et al. Experimental observations of heterogeneous strains inside a dual porosity sample under the influence of gas-sorption: a case study of fractured coal. Int J Coal Geol 2020: 103450.
[104] Wu Y, Liu J, Chen Z, Elsworth D, Pone D. A dual poroelastic model for CO2-enhanced coalbed methane recovery. Int J Coal Geol 2011;86(2–3):177–89.
[105] Sang G, Elsworth D, Miao X, Mao X, Wang J. Numerical study of a stress dependent triple porosity model for shale gas reservoirs accommodating gas diffusion in kerogen. J Nat Gas Sci Eng 2016;32:423–38.
[106] Wang C, Liu J, Feng J, Wei M, Wang C, Jiang Y. Effects of gas diffusion from fractures to coal matrix on the evolution of coal strains: experimental observations. Int J Coal Geol 2016;162:74–84.
[107] Wei M, Liu J, Shi R, Elsworth D, Liu Z. Long-term evolution of coal permeability under effective stresses gap between matrix and fracture during CO 2 injection. Transp Porous Media; 2019. p. 1–15.
[108] Liu J, Wang J, Chen Z, Wang S, Elsworth D, Jiang Y. Impact of transition from local swelling to macro swelling on the evolution of coal permeability. Int J Coal Geol 2011;88(1):31–40.